Presented at the 25th European PV Solar Energy Conference and Exhibition, 6-10 September 2010, Valencia, Spain

OPTIMISATION OF INDUSTRIAL N-TYPE SILICON SOLAR CELLS WITH ALUMINIUM-ALLOYED REAR EMITTER BY MEANS OF 2D NUMERICAL SIMULATION

Marc Rüdiger, Christian Schmiga, Michael Rauer, Martin Hermle and Stefan W. Glunz
Fraunhofer Institute for Solar Energy Systems (ISE)
Heidenhofstraße 2, 79110 Freiburg, Germany,
Tel: +49 (0) 761 4588 5921, Fax: +49 (0) 761 4588 9250, E-Mail: marc.ruediger@ise.fraunhofer.de

ABSTRACT: We present a detailed analysis on the optimisation of *n*-type silicon solar cells with aluminium-alloyed rear p^+ emitter for industrial applications by means of two-dimensional numerical simulation in order to identify the potential and the limiting factors for this cell concept. It is demonstrated, that the characteristic solar cell parameters can be simulated very well taking two-dimensional effects into account, leading to an excellent agreement compared to the measured results. Based on these simulations we show a complete and continuative study on the optimisation of this solar cell concept, analysing gradually three different regions of the solar cell. Firstly, the influence of the front side is investigated discussing different front surface fields and how they perform with an additional selective front surface field below the front contacts. Secondly, the influence of the base is discussed and how doping concentrations and pitch variations influence each other. Finally, the back side of this solar cell concept is analysed, how variations of the aluminium-alloyed rear p^+ emitters influence the cell performance.
Keywords: Simulation, Crystalline Silicon Solar Cells, *n*-type c-Si, Aluminium Emitter

1 INTRODUCTION

A comprehensive one-dimensional modelling of industrial *n*-type silicon solar cells with aluminium-alloyed rear p^+ emitter was already set up by Nagel and Schmiga et al. in 2006 [1], based on experimental cell results of 17% reported in Ref. [2] and predicting efficiencies of more than 18% by means of PC1D simulations. Since then a lot of effort has been spent to improve this solar cell concept by (i) optimising the rear Al-p^+ emitter, (ii) improving the phosphorus-diffused n^+ front surface field (FSF) covered by a SiN_x antireflection coating and (iii) applying aerosol-printed and silver-plated front contact fingers, leading to measured efficiencies of 18.2% in 2009 [3] and reaching the theoretical predictions.

Recently, we have achieved a new record-high efficiency of 19.3% [4] for our best industrial-type n^+np^+ solar cell on phosphorous-doped 10 Ωcm float-zone (FZ) silicon material by further improvements including the front surface field and applying an antireflection stack consisting of a 10 nm SiO_2 passivation layer and a 65 nm SiN_x antireflection coating. Due to these new improvements, the experimental results exceed by far the theoretical predictions made by Nagel et al.

Thus, in this work, we present a complete and continuative analysis on the optimisation of *n*-type silicon solar cells with aluminium-alloyed rear p^+ emitters, taking 2D effects of this cell concept into account, which have not been considered in previous work. For the 2D numerical simulations, Sentaurus Device (SD) from Synopsys [5] has been used.

2 COMPARISON: EXPERIMENT & SIMULATION

2.1 Solar Cell Structure

Our large-area n^+np^+ Al back junction solar cell is based on *n*-type phosphorus-doped 10 Ωcm FZ Si material and features a full-area screen-printed Al-p^+ rear emitter. The cell structure has an industrially feasible front side metallisation of an aerosol-printed and Ag-plated contact grid with a front side pitch d_{Pitch} of 1600 µm. The front surface is textured with random pyramids and has a phosphorus-n^+ FSF with $N_{\text{peak}} = 5 \cdot 10^{19}$ cm^{-3} and $R_{\text{sh}} = 90$ Ω/□. As antireflection coating a stack system consisting of a 10 nm SiO_2 and a 65 nm SiN_x layer is used. The Al-p^+ emitter is about 8 µm thick. A schematic sketch of the solar cell is shown in Fig. 1. Solar cell results are illustrated in Figs. 3 and 4. Further details are given in Ref. [4], presented at this conference.

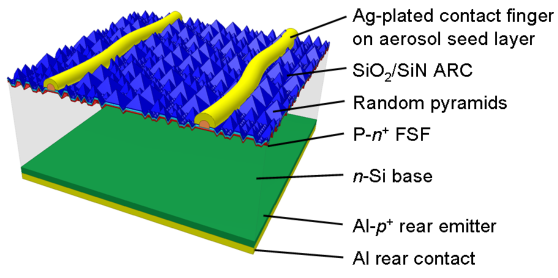

Figure 1: Schematic sketch of our n^+np^+ back junction silicon solar cell with full-area screen-printed aluminium-alloyed rear p^+ emitter, fabricated at Fraunhofer ISE.

2.2 Numerical Simulations

The numerical 2D simulations of the solar cell performance parameters have been done under standard operation conditions (25°C, 1-sun illumination intensity, AM1.5G spectrum) with the simulation tool Sentaurus Device from Synopsys [5]. The assumed parameters are summarised in Table I.

To model the electrical behaviour of the solar cell via the symmetry element shown in Fig. 2, but without selective FSF, the optics have been simulated separately in an optical symmetry element via ray tracing assuming upright pyramids (not shown). The transfer matrix method has been used to calculate the propagation of plane waves through the thin layers of the SiO_2/SiN anti-reflection coating (ARC). The results, 1D wavelength and penetration depth dependent generation profiles have

Table I: Parameters used for the simulation of our *n*-type Si solar cell featuring a full-area screen-printed Al-p^+ rear emitter and an aerosol-printed and Ag-plated front contact grid, described in section 2.1.

Parameter	Unit	Numerical value
Thickness d	µm	200
Front finger pitch w	µm	1600
Front contact finger width w_{finger}/Effective front contact finger width $w_{finger,eff}$	µm	60/80
Base doping concentration N_D	cm^{-3}	$4.5 \cdot 10^{14}$ (~ 10 Ωcm)
n^+ FSF profile	-	measured (see 2.1)
Al-p^+ emitter profile	-	measured (see 2.1)
Depth of Al-p^+ emitter d_{Al}	µm	8
Low level injection bulk lifetime τ_{eff}	ms	25 (see Fig. 6)
Reflection	-	adapted to measurement
Phong reflection R_{Phong}/Phong exponent w_{Phong}	-/-	0.7/4
Front surface recombination velocity $S_{0,FSF}$	cm/s	$4 \cdot 10^3$ (cf. [6])
Surface recombination velocity at contacts $S_{0,contact}$	cm/s	$1 \cdot 10^7$
Series resistance for contacts, fingers and busbars $R_{S,ext}$	Ωcm^2	0.6

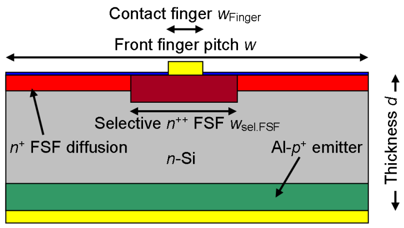

Figure 2: Schematic sketch of an n^+np^+ Al back junction Si solar cell with selective FSF. The symmetry element used for simulations is half of the shown element.

been coupled into the 2D electrical device simulation. Internal reflection at the rear side of the cell has been accounted for by the Phong-model [7], leading to very good agreement of the simulated and the experimentally measured reflection curves in the range above 360 nm (cf. Fig. 3). The difference in the reflection curves can be directly seen as well in the *EQE* characteristics. But due to the small photon density of the incident light below $\lambda = 360$ nm counting 1.5% of the whole photon flux of the AM1.5G-spectrum there is a negligible influence on the simulation results.

A front finger width $w_{finger} = 60$ µm could be measured at the solar cell samples. To account for the geometrical shadowing losses of around 6% including the busbars an effective finger width $w_{finger,eff}$ has been

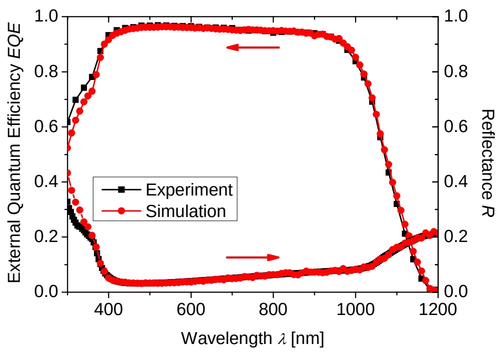

Figure 3: External quantum efficiency and reflection of measurement and simulation for our n^+np^+ Al back junction Si solar cell. Excellent agreement could be achieved for wavelengths above 360 nm. Due to the small photon density below 360 nm in the AM1.5G-spectrum there is a negligible influence on the simulation results.

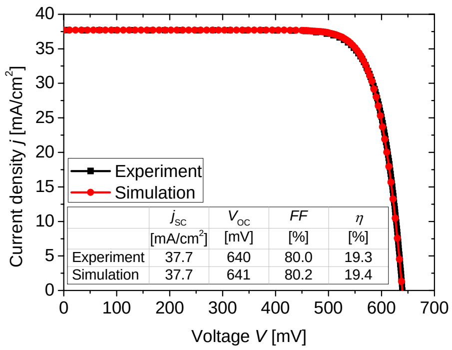

Figure 4: *IV*-curve and solar cell performance parameters of measurement and simulation for our n^+np^+ Al back junction Si solar cell. Excellent agreement could be achieved.

introduced. Due to the rounded shape of the silver plated contacts, 14% [8] of the reflected light at the metallisation surface is additionally coupled into the device contributing to the generation current. Thus, a resulting effective finger width $w_{finger,eff} = 80$ µm has been assumed for simulations. To avoid confusions, in continuation only the front finger width w_{finger} will be mentioned.

The series resistance $R_{S,int}$ within the device is accounted for in the numerical simulation, whether for the series resistance caused by the contacts, fingers and busbars, an additional external $R_{S,ext}$ of 0.6 Ωcm^2 has been added.

In the past, simulating Al-p^+ emitters for *n*-type or back surface fields (BSFs) for *p*-type Si solar cells, respectively, has been challenging, because using the experimentally determined Al profile for device modelling led to far too low saturation current densities $j_{0,Al}$ resulting first of all in overestimated V_{oc} values. Thus, Altermatt et al. [9] proposed a lifetime parameterisation for the Shockley-Read-Hall (SRH) lifetime $\tau_{SRH}(N_A)$ depending on the acceptor concentration N_A. In this work, a new method to describe Al-p^+ emitters/BSFs has been applied, which will be described elsewhere soon.

As can be seen in Fig. 4, an excellent agreement of the solar cell parameters of the calculated and experimentally determined results could be achieved with this model.

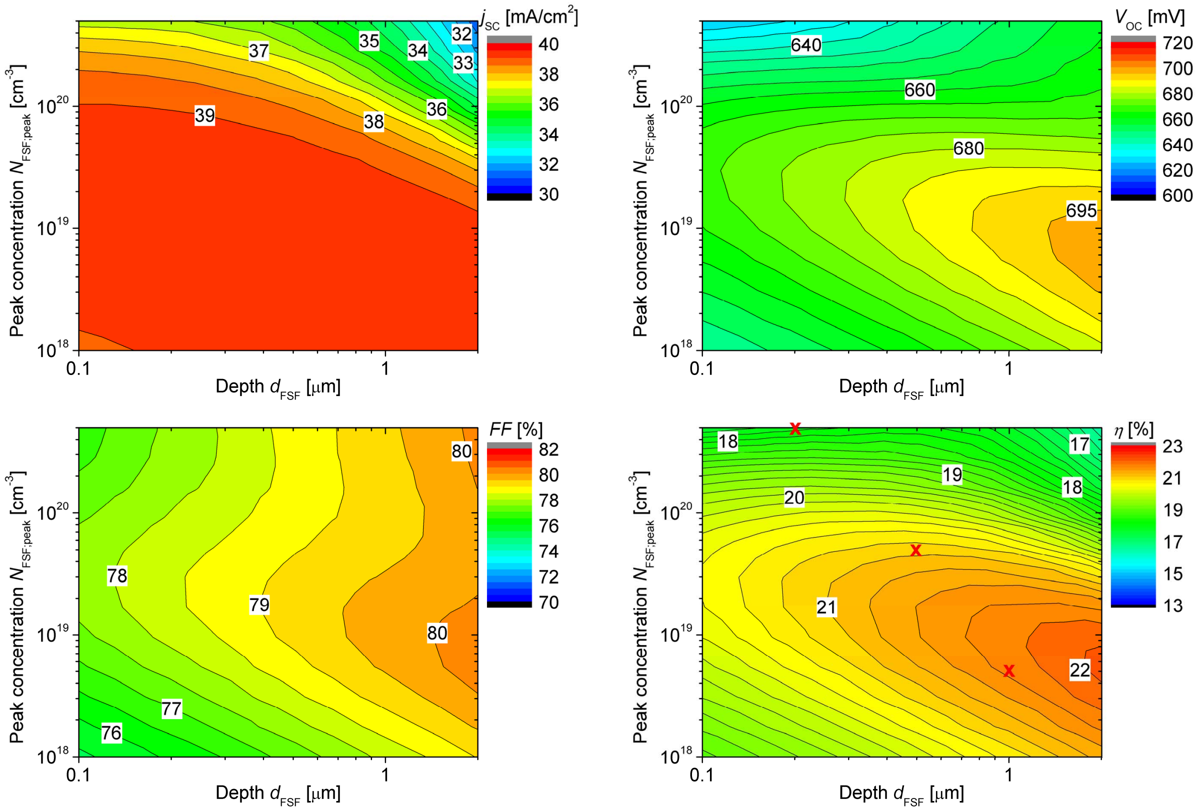

Figure 5: Variation of the FSF peak concentration $N_{\mathrm{FSF,peak}}$ and the profile depth d_{FSF} of our n^+np^+ Al back junction Si solar cell with a base doping concentration $N_{\mathrm{D}} = 4.5 \cdot 10^{14}$ cm^{-3} **(ρ = 10 Ωcm)** without assuming a selective FSF. Shown are the cell parameters short-circuit current density j_{sc}, open-circuit voltage V_{oc}, fill factor *FF* and efficiency η for a cell thickness $d = 200$ µm, a front finger pitch $w = 1600$ µm and a contact width $w_{\mathrm{finger}} = 60$ µm. Note, that the rear side (emitter profile and contact conditions) has been assumed as a perfect rear side in order to focus on the FSF properties. The three red crosses (bottom, right) indicate the profile parameters used for further variations (cf. Table II).

3 ANALYSIS OF CELL CONCEPT

3.1 Parameters

Based on the simulations in section 2 our n^+np^+ Al back junction Si solar cell concept is analysed in detail. A schematic sketch of the modelled symmetry element is given in Fig. 2. For simplicity the FSF is assumed in continuation as an error function profile and the Al-p^+ emitter as an abrupt profile with an acceptor surface concentration of $N_{\mathrm{A}} = 1 \cdot 10^{18}$ cm^{-3} exponentially increasing to $3 \cdot 10^{18}$ cm^{-3} at a depth of 8 µm, which is quite similar to the measured profile used in section 2.2. The used profile can be seen in Fig. 11 (above, inset). As standard geometry for the front finger pitch, contact finger width and wafer thickness, data as shown in Table I have been assumed.

By varying the FSF peak concentrations a change in the surface recombination velocity $S_{0,\mathrm{front}}$ has to be accounted for as well. Thus, a parameterisation of S_0 dependent on the surface peak concentration $N_{\mathrm{FSF,peak}}$ for phosphorus-doped Si surfaces proposed by Cuevas et al. [6] has been applied:

$$S_0(N_{\mathrm{FSF,peak}}) = 70 \cdot \frac{N_{\mathrm{FSF,peak}}}{7 \cdot 10^{17}} \qquad (1)$$

For the minority capture time constants τ_{p0} of the base material, lifetimes of Kerr et al. [10] have been assumed, which can be seen in Fig. 6. For the defect parameters of the SRH-model, a defect level $E_{\mathrm{t}} = E_{\mathrm{i}}$ and a symmetry factor $k = 1$ have been assumed.

Three different FSF error function profiles are investigated in detail, chosen due to their contactability with different metallisation techniques, which are summarized in Table II. Profiles (a) and (b) are both examples for industrially relevant $POCl_3$-diffused FSF profiles. While (a) is a typical profile used in mass production, (b) represents a profile after a drive-in process, which is quite similar to the via electrochemical capacitance voltage (ECV) measured FSF profile of our 19.3% solar cell presented in section 2. While profile (b)

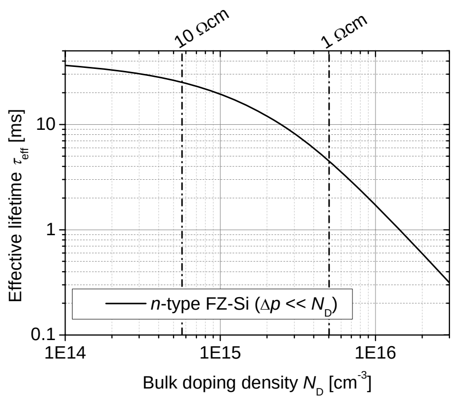

Figure 6: Effective lifetimes $\tau_{\mathrm{eff}}(N_{\mathrm{D}})$ of *n*-type FZ Si material dependent on the bulk doping density N_{D} [10].

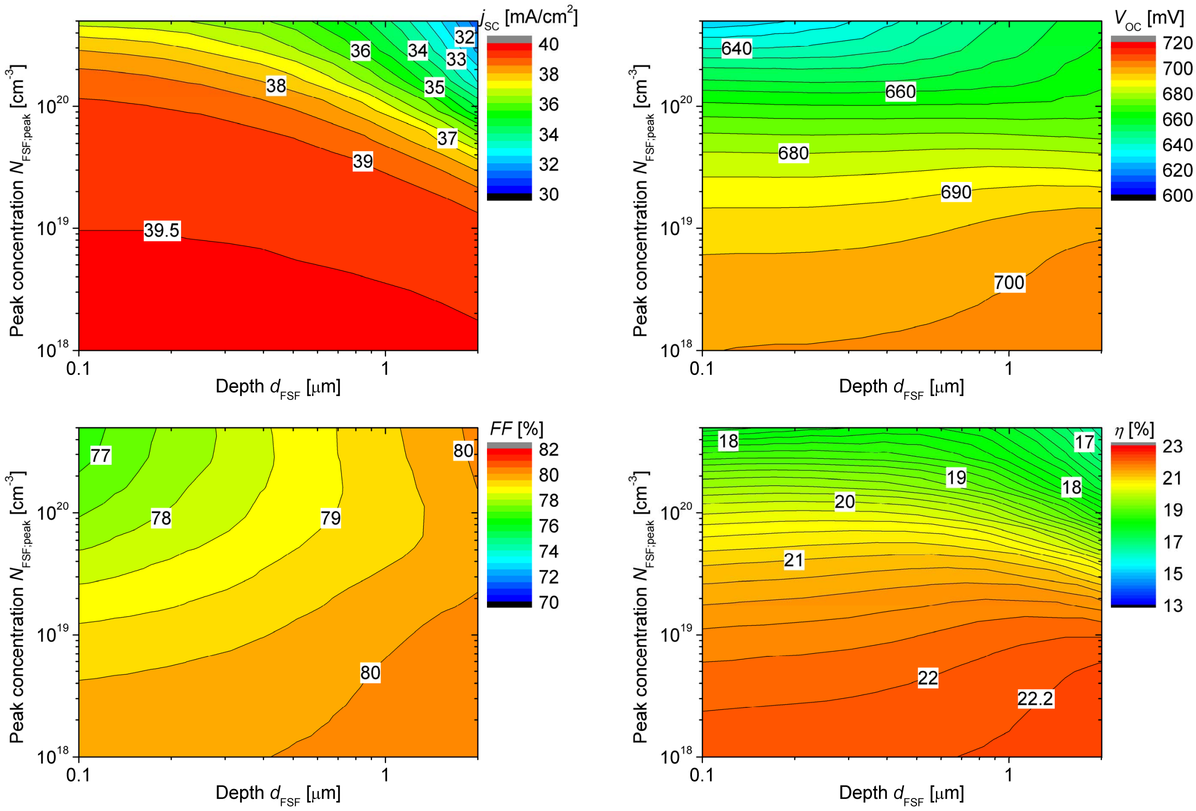

Figure 7: Variation of the FSF peak concentration $N_{FSF,peak}$ and the profile depth d_{FSF} of our n^+np^+ Al back junction Si solar cell with a base doping concentration $N_D = 4.5 \cdot 10^{14}$ cm^{-3} **(ρ = 10 Ωcm) with selective FSF (a)** (cf. Table II) with $w_{sel.FSF} = 100$ µm. Shown are the cell parameters short-circuit current density j_{sc}, open-circuit voltage V_{oc}, fill factor FF and efficiency η for a cell thickness $d = 200$ µm, a front finger pitch $w = 1600$ µm and a contact width $w_{Finger} = 60$ µm. Note, that the rear side (emitter profile and contact conditions) has been assumed as a perfect rear side in order to focus on the FSF properties.

can only be contacted via advanced metallisation techniques like aerosol- or inkjet-printing in combination with plated contacts due to the lower N_{peak}, profile (a) can also be contacted via a standard screen-printing process. The third profile (c) reflects a $POCl_3$-diffused profile for high-efficiency applications, but could also be achieved on an industrial level e.g. via very promising techniques like ion implantation, requiring an adequate metallisation.

3.2 Analysis of Front Surface Field (FSF)

To determine the influence of different FSFs, an error function profile has been varied in peak concentration N_{peak} and profile depth d_{FSF}. The surface recombination velocities are varied according to Eq. 1, respectively. The

Table II: Three different FSFs have been investigated in detail in this work. Profile (a) can be contacted via a standard screen-printing process, while profile (b) can be only contacted via advanced metallisation techniques like aerosol- or inkjet-printing in combination with plated contacts, due to the lower peak concentration N_{peak}.

Profile	$N_{FSF,peak}$ [cm^{-3}]	d_{FSF} [µm]	R_{sh} [Ω/□]	Metallisation type
(a)	$5 \cdot 10^{20}$	0.2	55	"standard"
(b)	$5 \cdot 10^{19}$	0.5	140	"advanced"
(c)	$5 \cdot 10^{18}$	1.0	280	"high η"

cell geometry is set up like explained in section 3.1, except the rear side. In order to focus on the FSF properties, the back side emitter and the back contact have been assumed as perfect, featuring a very lowly doped emitter profile and ohmic contacts without any surface recombination.

In Fig. 5 the FSF variations can be seen for a base doping concentration $N_D = 4.5 \cdot 10^{14}$ cm^{-3} (ρ = 10 Ωcm). Taking a look at the short-circuit current densities indicates high values of ~ 39 mA/cm^2 over a broad range, decreasing turning to very highly doped profiles, mainly due to increased Auger recombination losses. At high peak doping concentrations, V_{oc} is mainly decreasing due to increasing saturation current densities $j_{0,FSF}$ reaching 200 fA/cm^2 above $N_{FSF,peak} = 1 \cdot 10^{20}$ cm^{-3} and rising to a multiple of this value affecting the fill factor and thus the efficiency as well. In case of FSFs becoming lower surface-doped (below $N_{FSF,peak} = 1 \cdot 10^{19}$ cm^{-3}), it seems, that the majority carrier current flows more and more through the bulk material due increasing sheet resistances in the FSF, causing series resistance problems, because of the low doping density in 10 Ωcm bulk material. Additionally, the minority carriers in the base material are less and less shielded from the highly recombination active front contact, leading to a strong decrease of the fill factor and thus the efficiency. Our simulations lead to the conclusion that the best solar cell efficiencies can be achieved using very deep diffused profiles with peak concentrations around 10^{19} cm^{-3}.

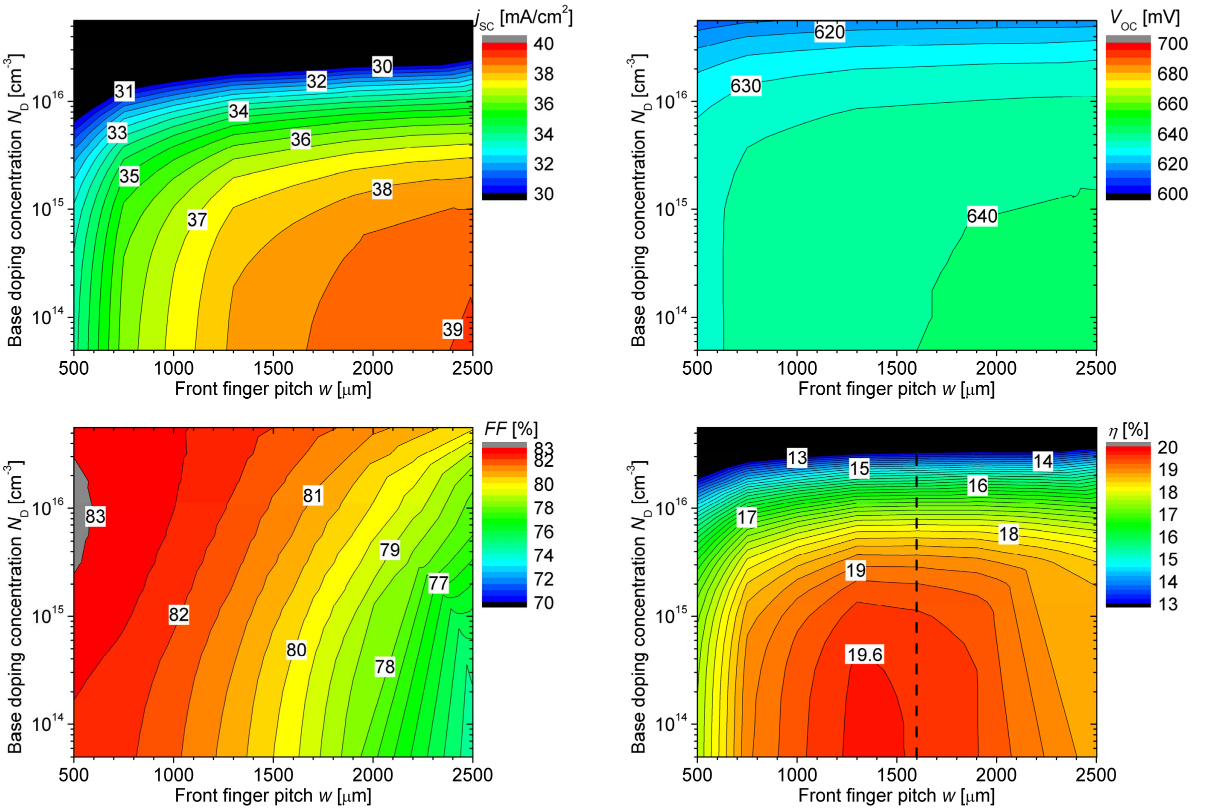

Figure 8: Variation of the base doping concentration N_D depending on the front finger pitch w of our n^+np^+ Al back junction Si solar cell. Shown are the cell parameters short-circuit current density j_{sc}, open-circuit voltage V_{oc}, fill factor *FF* and efficiency η for a cell thickness $d = 200$ µm and a contact width $w_{\text{finger}} = 60$ µm. For the FSF profile (b) from Table II has been used and an Al-p^+ emitter with a depth $d_{\text{Al}} = 8$ µm has been assumed. The influence of different FSFs and combinations with selective FSFs on η can be seen in Fig. 9 for a fixed w (indicated by the dashed black line, bottom right).

Introducing an additional selective FSF (Table II, (a)) with $d_{\text{sel.FSF}} = 100$ µm below the front contacts leads to the results shown in Fig. 7. By comparing with Fig. 5 (same setup, but without selective FSF), it can be clearly seen, that no difference in the results occurs for FSFs with peak concentrations above around $5 \cdot 10^{19}$ cm^{-3}, due to a good shielding of the minority carriers from the highly recombination active front side contact, even without a selective FSF. Below $5 \cdot 10^{19}$ cm^{-3}, the selective FSF acts as excellent minority carrier barrier and thus leading to increasing V_{oc} values the lower $N_{\text{FSF,peak}}$ becomes. Interestingly, no *FF* loss can be seen any more for very lowly surface-doped FSFs, leading to the conclusion that the conductability of 10 Ωcm *n*-type FZ Si bulk material does not limit the lateral current density, as assumed before. As a result η increases continuously by decreasing $N_{\text{FSF,peak}}$, due to a constantly decreasing saturation current density in the FSF.

3.3 Influence of Bulk Material and Pitch

In Fig. 8 the base doping concentration of our n^+np^+ Al back junction Si solar cell is being varied in a broad range, covering resistivities from 0.1 Ωcm until nearly 100 Ωcm. Additionally the influence of the front finger pitch w is shown. At the rear side an 8 µm deep Al-p^+ emitter and at the front side a FSF with $N_{\text{FSF,peak}} = 5 \cdot 10^{19}$ cm^{-3} (Table II, (b)) have been included in the simulations. The lifetimes have been accounted for according to Fig. 6.

Going to higher doping concentrations N_D, V_{oc} and j_{sc} are decreasing continuously, even more pronounced above $N_D > 1 \cdot 10^{16}$ cm^{-3}, but by far less than it was observed before [1]. As could be observed in Ref. [11], this effect results from a strong increase of the minority-carrier concentration in the FSF with increasing bulk doping concentration. This higher minority-carrier concentration in the FSF leads to a higher recombination rate and, thus, to a lower charge collection probability of the minority carriers at the rear side contact, which results in the decreasing j_{sc}. Obviously j_{sc} is decreasing as well going to smaller front finger pitches, due to the constant finger width $w_{\text{Finger}} = 60$ µm. The smaller w, the more decreases the fraction of incident light coupling into the solar cell.

A contrarily behaviour can be observed looking at the fill factor. The wider w, the more pronounced lateral current effects become. As a consequence of a continuously increasing series resistance, the *FF* decreases. Due to contrary behaviour of j_{sc} and *FF*, a maximum in the efficiency depending on the pitch appears in the range slightly below the pitch of our realised solar cell considered in section 2.

The influence of different FSFs depending on the base doping concentration N_D can be seen in Fig. 9 by holding $w = 1600$ µm fixed (indicated by the black dashed line in Fig. 8). Above variations for "advanced" metallisation techniques with printed seed layers and plated contacts are shown, allowing contacting

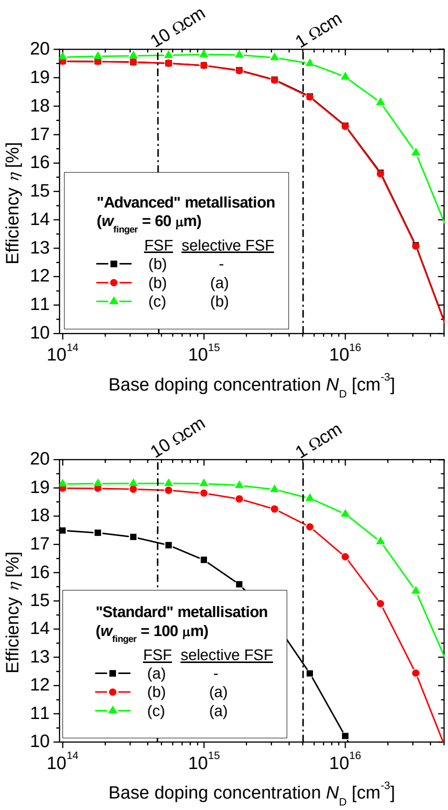

Figure 9: Influence of different FSFs with and without selective diffusions below the contacts ("selective FSF"). Above variations for "advanced" metallisation techniques are shown, allowing contacting lowly doped surfaces and achieving narrower finger widths. Below results for standard metallisation techniques like screen-printing are shown. The profile abbreviations can be seen in Table II (w = 1600 µm).

phosphorus-doped surfaces with concentrations down to $N_D = 5{\cdot}10^{19}$ cm^{-3} and achieving narrower finger widths of w_{finger} = 60 µm. Below results for "standard" metallisation techniques like screen-printing are shown, necessitating surface concentrations of approximately $5{\cdot}10^{20}$ cm^{-3} and being limited to finger widths of 100 µm ($w_{finger,eff}$ = 120 µm, cf. section 2.2). The profile abbreviations can be seen in Table II.

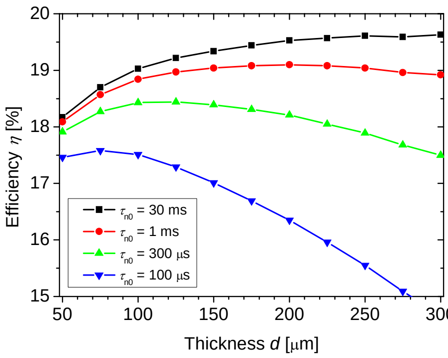

Figure 10: Influence of the wafer thickness d and bulk minority carrier lifetime τ on the efficiency η of our n^+np^+ Al back junction Si solar cell (10 Ωcm). A front finger pitch w = 1600 µm has been assumed, with w_{finger} = 60 µm and d = 200 µm.

Whereas in Fig. 9 (above) profile (b) as FSF has a strong dependence on the base doping concentration (absolute reduction of η by 1% absolute, comparing 1 and 10 Ωcm), the efficiency especially on 1 Ωcm material can be significantly increased by reducing $N_{FSF,peak}$ and implementing a selective FSF (combination (c) & (b)), which presently might not be industrially realisable with low cost processes.

Due to an increased shadowing loss by the use of standard screen-printing metallisation (Fig. 9, below) the efficiency is overall decreased by about 0.5% absolute (which can be seen by comparing profile combination (b) & (c) for both metallisation types). A homogeneous FSF with profile (a) leads to a strong decrease of η, due to significantly increased Auger recombination within the FSF. Here the use of a selective FSF, industrially feasible with profile (a), enhances the solar cell performance by far and is highly recommended.

Until now, effective minority carrier lifetimes τ_{eff} for n-type FZ Si have been assumed. The behaviour of the cell performance by reducing τ_{eff} can be exemplarily seen in Fig. 10. For very high lifetimes above 10 ms the optimal thickness is beyond 300 µm, due to an enhanced absorption of incident photons. At τ = 1 ms and below the diffusion length limits the current and thus the efficiency, because in contrast to p-type Si solar cells the minority carriers, predominantly generated at the front side of the wafer, have to diffuse to the rear side passing the entire wafer thickness before reaching the junction.

3.4 Analysis of Rear Side

As has been reported recently [3,12,13], a significant improve of V_{oc} can be achieved by passivating the

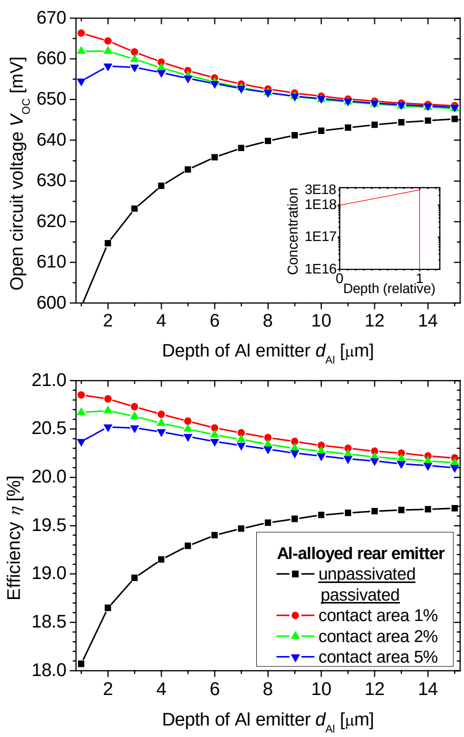

Figure 11: Variation of the thickness d_{Al} of the full-area screen-printed aluminium-alloyed rear emitter. Shown are the open-circuit voltage V_{oc} and efficiency η for non-passivated and passivated rear emitters, the latter with varying contact metallisation coverage of the rear side.

surface of the full-area screen-printed aluminium-alloyed rear emitter. For modelling this behaviour, a fully contacted unpassivated rear side with $S_{0,\mathrm{rear,unpass}} = 10^7$ cm/s has been compared to an n^+np^+ cell with a perfectly passivated rear side ($S_{0,\mathrm{rear,pass}} = 0$ cm/s) and point contacts. The rear side pitch w_{rear} has been set to 530 µm. Additionally, the contact metallisation fraction has been varied, as can be seen in Fig. 11.

Whereas V_{oc} decreases with decreasing thickness of the Al-p^+ emitter due to an increasing influence on the recombination of minority carriers at the unpassivated rear side, for passivated rear side Al-p^+ emitters the behaviour inverts, resulting in increasing V_{oc} values with decreasing thicknesses. Metallisation coverage fractions of 1% are normally used. Increasing this fraction results in a decrease of V_{oc} mainly for relatively thin Al emitters (full-area screen-printed aluminium-alloyed rear emitters usually have thicknesses around 6 - 10 µm, depending on the amount of Al deposited).

In addition, j_{sc} is significantly influenced due to a rear side passivation as well. The passivation enhances the reflection properties by 16% ($R_{\mathrm{Phong}} = 0.86$) at the rear side in the long wavelength range above $\lambda = 1000$ nm leading to an increased j_{sc} of 1.5 mA/cm^2 (not shown).

4 CONCLUSIONS

In this work, we present a detailed analysis on the optimisation of *n*-type silicon solar cells with aluminium-alloyed rear p^+ emitter for industrial applications by means of two-dimensional numerical simulation. To verify the simulation results, it could be shown, that the cell performance parameters of an n^+np^+ Al back junction solar cell based on *n*-type phosphorus-doped 10 Ωcm FZ silicon material with 19.3% efficiency could be simulated with excellent accordance.

In order to identify the efficiency limiting factors we modelled the cell concept by sequentially focussing on effects from the front side, bulk material and back side.

The following improvements of our presented cell concept could be observed:

(i) Lowering the front finger pitch slightly might increase the efficiency by 0.1% absolute.

(ii) A further drive-in of the FSF, which lowers the peak concentration, would result in an efficiency increase, even more effective with the use of a selective FSF locally below the front metallisation.

(iii) The implementation of an additional passivation layer on the surface of the rear Al-p^+ emitter might lead to enhanced reflection conditions and thus an increase in the short-circuit current density of 1.5 mA/cm^2. In combination with a significant V_{oc} enhancement, the efficiencies might potentially increase by 1% absolute and beyond.

With these realistic improvements, we are confident that an efficiency of more than 20% can been obtained for our investigated industrial n^+np^+ Al back junction Si solar cell in the near future.

5 ACKNOWLEDGEMENTS

The authors would like to thank Gergö Létay and Stefan Odermatt from Synopsys for their support and Peter Kailuweit, Christian Reichel, Martin Bivour and all colleagues from Fraunhofer ISE for fruitful discussions. This work has been financially supported by Bosch Solar Energy.

6 BIBLIOGRAPHY

[1] H. Nagel, C. Schmiga, B. Lenkeit, G. Wahl and W. Schmidt, Proc. 21st EU PVSEC, Dresden, Germany, 2006, p. 1228-34.

[2] C. Schmiga, H. Nagel, J. Schmidt, Progress in Photovoltaics: Research and Applications **14,** p. 533-9 (2006).

[3] C. Schmiga, M. Hörteis, M. Rauer, K. Meyer, J. Lossen, H.-J. Krokoszinski, M. Hermle and S. W. Glunz, Proc. 24th EU PVSEC, Hamburg, Germany, 2009, p. 1167-70.

[4] C. Schmiga, M. Rauer, M. Rüdiger, K. Meyer, J. Lossen, H.-J. Krokoszinski, M. Hermle and S. W. Glunz, *Aluminium-doped p^+ silicon for rear emitters and back surface fields: Results and potentials of industrial n- and p-type solar cells*, this conference

[5] Synopsys, TCAD (2010).

[6] A. Cuevas, G. Giroult-Matlakowski, P. A. Basore, C. DuBois and R. R. King, Waikoloa, Hawaii, USA, 1994 (IEEE; New York, NY, USA), p. 1446-9.

[7] J. Foley, A. van Dam, S. Feiner and J. Hughes, (Addison-Wesley Publishing Company, Amsterdam, 1990).

[8] R. Woehl, M. Hörteis and S. W. Glunz, Advances in OptoElectronics, Vol. 2008, 759340 (2008).

[9] P. Altermatt, S. Steingrube, Y. Yang, C. Sprodowski, T. Dezhdar, S. Koc, B. Veith, S. Herrman, R. Bock, K. Bothe, J. Schmidt and R. Brendel, Proc. 24th EU PVSEC, Hamburg, 2009, p. 901-6.

[10] M. J. Kerr and A. Cuevas, Journal of Applied Physics **91,** 2473-80 (2002).

[11] M. Hermle, F. Granek, O. Schultz and S. W. Glunz, Journal of Applied Physics **103,** 054507 (2008).

[12] M. Rauer, C. Schmiga, M. Hermle and S. W. Glunz, Proc. 24th EU PVSEC, Hamburg, Germany, 2009, p. 1059-62.

[13] M. Rauer, C. Schmiga, M. Hermle and S. W. Glunz, Physica Status Solidi A, Vol. 207, 5, p. 1059 (2009).